Signaling by the integrated stress response kinase PKR is fine-tuned by dynamic clustering

Francesca Zappa[1,*], Nerea L. Muniozguren[1], Jose Carlos Ponce-Rojas[1], Diego Acosta-Alvear[1,*]

[1]Department of Molecular, Cellular and Developmental Biology, University of California, Santa Barbara, Santa Barbara, CA 93106

*Correspondence: fzappa@ucsb.edu, daa@lifesci.ucsb.edu

Abstract

The double-stranded RNA sensor kinase PKR is one of four integrated stress response (ISR) sensor kinases that phosphorylate the alpha subunit of the eukaryotic initiation factor 2 (eIF2α) in response to stress. The current model of PKR activation considers the formation of back-to-back PKR dimers as a prerequisite for signal propagation. Here we show that PKR signaling involves the assembly of dynamic PKR clusters. PKR clustering is driven by ligand binding to PKR's sensor domain and by front-to-front interfaces between PKR's kinase domains. PKR clusters are discrete, heterogeneous, autonomous coalescences that share some protein components with processing bodies. Strikingly, eIF2α is not recruited to PKR clusters, and PKR cluster disruption enhances eIF2α phosphorylation. Together, these results support a model in which PKR clustering buffers downstream signaling, which may enable proofreading the ISR.

Introduction

The integrated stress response (ISR) is an evolutionarily conserved stress signaling network that adjusts the cellular biosynthetic capacity according to need. Four stress sensor kinases govern the mammalian ISR: GCN2 (general control nonderepressible 2), which detects uncharged tRNAs; HRI (heme-regulated inhibitor), which detects heme deficiency, redox imbalances and acts as signaling relay for mitochondrial stress; PERK (PKR-like ER kinase) which detects protein-folding perturbations in the lumen of the ER, or "ER stress"; and PKR (protein kinase RNA-activated), which detects double-stranded RNA (dsRNA). The ISR kinases phosphorylate the eukaryotic translation initiation factor eIF2—a heterotrimeric GTPase—on a single serine (Ser51) of its alpha subunit (eIF2α), causing a temporary shutdown of protein synthesis. Global translational repression by eIF2α phosphorylation is coupled to the selective synthesis of specific proteins, including the transcription factors ATF4 and CHOP. Through this bipartite mechanism, the ISR reprograms the transcriptome and proteome (Costa-Mattioli and Walter, 2020).

PKR is the most recently evolved ISR kinase (Rothenburg et al., 2009). It has known roles in innate immunity (Pindel and Sadler, 2011; Cole, 2007) and in various neurological disorders characterized by cognitive decline (Peel, 2001; Bando et al., 2005; Hugon et al., 2017; Zhu et al., 2019). PKR detects viral and endogenous dsRNAs, including leaked mitochondrial transcripts, nuclear dsRNAs, and Alu-repeat RNAs (Ben-Asouli et al., 2002; Elbarbary et al., 2013; Kim et al., 2014; Youssef et al., 2015; Kim et al., 2018a; Chung et al., 2018; Kim et al., 2020; Lee et al., 2020a). Structurally, PKR is composed of two dsRNA binding domains (RBDs) and a kinase domain adjoined to the RBDs by a ~100 aminoacid unstructured linker (Sadler and Williams, 2007). Like the rest of the ISR kinases, PKR forms back-to-back dimers sufficient for signal propagation upon activation (Maia de Oliveira et al., 2020; Dey et al., 2005; Lavoie et al., 2014; Cui et al., 2011; Dar et al., 2005). However, recent crystallographic evidence indicates that PKR could form high-order associations through front-to-front interfaces in PKR's kinase domain (Mayo et al., 2019). This observation suggests that PKR forms high-order

associations in living cells, similar to the ER stress sensors PERK and IRE1 (Carrara et al., 2015; Korennykh et al., 2009; Li et al., 2010; Bertolotti et al., 2000; Cui et al., 2011; Belyy et al., 2021) and the innate immunity effector RNase L (Han et al., 2012). These independent lines of evidence hint at a conserved mechanistic principle of dynamic clustering of stress sensors upon activation.

To gain insights into PKR's activation mechanism, we used microscopy-based analyses to examine PKR's behavior in living cells. Our approaches revealed that upon activation, PKR assembles into autonomous, dynamic cytosolic clusters that are devoid of eIF2α, and that preventing PKR cluster formation enhanced PKR signaling. Taken together, our results highlight an unexpected feature of the ISR in which compartmentalization modulates PKR-eIF2α interactions to fine-tune signaling.

Results

PKR forms dynamic clusters upon activation

To investigate the behavior of PKR in living cells, we introduced the red fluorescent protein mRuby in the interdomain linker of human PKR (Fig. S1A). We used this construct to generate a stable H4 neuroglioma cell line expressing mRuby-PKR on the background of CRISPRi-mediated knockdown of endogenous PKR. The level of mRuby-PKR in these cells was approximately 1.8-fold when compared to endogenous PKR (Fig. S1B, C). We chose H4 cells because maladaptive PKR signaling has been observed in several neuropathologies (Martinez et al., 2021). To prevent cross-talk between mRuby-PKR and endogenous PKR, we depleted the latter using CRISPRi knockdown (Fig. S1B, C). Treatment of these cells with poly I:C, a synthetic dsRNA mimetic and potent PKR activator (Balachandran et al., 2000), led to the formation of mRuby-PKR clusters within ~20 minutes (Fig. 1A, B; Video 1), and immunofluorescence analyses showed that mRuby-PKR in the clusters was phosphorylated (Fig. 1D). The number of mRuby-PKR clusters per cell averaged 14.7±7.93, and their size ranged from 0.22 µm to 5 µm in diameter (Fig. S1D). Live-cell imaging analyses revealed that PKR

clusters coalesced and segregated within minutes, indicating dynamic behavior (Fig. 1C; Video 1).

Next, we investigated whether mRuby-PKR would exhibit the same behavior in response to natural dsRNAs. PKR's best-known role is to detect viral dsRNAs, including those generated by the measles virus (MV) (García et al., 2007). Infection of H4 cells expressing mRuby-PKR with a mutant MV strain (MV^{CKO}) that potently activates PKR (Okonski and Samuel, 2013; Toth et al., 2009; Pfaller et al., 2014), induced mRuby-PKR cluster assembly within ~38 hours, which is consistent with the timeline of viral replication tracked with GFP signal (Pfaller et al., 2014) (Fig. 1E, F). PKR has also been shown to be activated by endogenous dsRNAs, including nuclear dsRNAs that are released into the cytosol upon disruption of the nuclear envelope during mitosis (Kim et al., 2014; Youssef et al., 2015; Kim et al., 2018b). In agreement with these findings, we observed the formation of mRuby-PKR clusters in H4 cells undergoing mitosis (Fig. 1G, arrowheads; Video 2).

The formation of PKR clusters suggests a form of compartmentalization that is evocative of biological coacervates (Fare et al., 2021). To address whether PKR clusters exhibit coacervate-like behavior, we took two complementary approaches. First, we treated cells in which we induced mRuby-PKR clustering with 1,6-hexanediol, a hydrophilic alcohol that dissolves coacervates (Kroschwald et al., 2015; Alberti et al., 2019). Treatment with 1,6-hexanediol dissolved mRuby-PKR clusters within ~15 minutes (Fig. 1H). Second, to study the dynamics of mRuby-PKR clustering, we performed fluorescent recovery after photobleaching (FRAP) analyses. FRAP analyses revealed an exchange rate of 3.93s ±0.18 SEM between the cluster and cytosolic mRuby-PKR pools (Fig. S1E, F). Notably, mRuby-PKR fluorescence in the clusters was only recovered to ~50% of its initial intensity (Fig. 1I), indicating that PKR clusters consist of at least two different PKR pools, one that quickly exchanges with the cytosol and another one that is stably recruited into the cluster. Taken together, these results suggest that PKR signaling entails the formation of dynamic coalescences that are reminiscent of coacervates.

PKR clusters are autonomous entities

Being an RNA-binding protein, it is not surprising that PKR has been observed in association with processing bodies (PBs) and stress granules (SGs) (Reineke and Lloyd, 2015; Reineke et al., 2015; Hebner et al., 2006; Dougherty et al., 2014), which are heterogeneous cytosolic liquid-like RNA granules that regulate mRNA metabolism (Protter and Parker, 2016; Luo et al., 2018). These observations suggest that PKR partitions to PBs and SGs upon activation and during signaling. Poly I:C treatment of H4 cells expressing mRuby-PKR induced SG formation, as evidenced by the assembly of G3BP1 foci, a canonical SG marker (Fig. 2A). However, mRuby-PKR clusters failed to colocalize with G3BP1 in these experimental conditions (Fig. 2A). Immunofluorescence analyses of poly I:C treated H4 cells expressing mRuby-PKR indicated that most–but not all–mRuby-PKR clusters colocalized with Edc3, a canonical PB marker (Fig. S2A). Moreover, we found an inverse correlation between PKR cluster size and Edc3 colocalization, wherein PKR clusters exceeding an average size of 2.50 µm ±0.29 in diameter consistently failed to colocalize with Edc3 (Fig. S2A). Imaging analyses in fixed cells co-expressing mRuby-PKR and GFP-Dcp1a, a fluorescently-tagged canonical PB marker, showed the same colocalization pattern (Fig. S2B). Thus, mRuby-PKR clusters colocalized in part with PBs but not SGs markers.

To gain insights into the dynamics of PKR-PB associations, we performed super-resolution live imaging microscopy in cells expressing mRuby-PKR and GFP-Dcp1a, (Fig. 2B; Video 3). These experiments revealed that some mRuby-PKR clusters colocalize with GFP-Dcp1a upon poly I:C stimulation (Fig. 2B), yet ejection of mRuby-PKR from GFP-Dcp1a-containing clusters occurred shortly after (~15 minutes after assembly, Fig. 2B; Video 3). However, mRuby-PKR and GFP-Dcp1a coalescences remained in apposition after de-mixing, indicating potential tethering (Fig. 2B; Video 3). Furthermore, these experiments showed that ~50% of mRuby-PKR clusters consistently failed to colocalize with GFP-Dcp1a (Fig. 2C), suggesting the existence of an autonomous pool of PKR clusters devoid of GFP-Dcp1a. The discrepancy between the

extent of PB and PKR cluster colocalization obtained through super-resolution live-cell imaging and conventional imaging carried out in fixed cells can be attributed to the effects of the fixative we used and further substantiates that PKR clusters are highly dynamic.

The interconnectivity between PKR clusters and PBs prompted us to investigate their potential interdependence. To this end, we employed two orthogonal approaches. First, we treated mRuby-PKR expressing H4 cells with cycloheximide (CHX), a translation inhibitor that leads to polysome stabilization and depletion of PBs (Fig. S2.1C and Sheth and Parker, 2003; Cougot et al., 2004). Second, we knocked down 4E-T, the transporter of the mRNA cap-binding protein eIF4E, by RNA interference (RNAi), which also led to PB depletion (Fig. S2.1C,E and Andrei et al., 2005). Neither CHX nor 4E-T RNAi hampered mRuby-PKR cluster assembly or affected their dynamic behavior upon poly I:C treatment (Fig. 2D-E). Surprisingly, both CHX treatment and 4E-T RNAi led to the recruitment of Edc3 to mRuby-PKR clusters (Fig. 2F), and CHX induces redistribution of 4E-T—which localizes to PBs—into mRuby-PKR clusters upon poly I:C administration (Fig. S2.1D), suggesting that PKR clusters are capable of recruiting PB components.

Next, we investigated potential associations between PKR clusters and membrane-bound organelles. Immunofluorescence analyses in H4 cells expressing mRuby-PKR treated with poly I:C revealed that mRuby-PKR clusters did not associate with lysosomes, endosomes, autophagosomes, peroxisomes, or the cis-medial Golgi apparatus (Fig. S2.2A). By contrast, live-cell imaging analyses revealed transient interactions with the mitochondrial network and the endoplasmic reticulum (ER) (Fig. S2. 2B, Videos 4,5). These observations are consistent with recent reports suggesting that PKR localizes to mitochondria and that it senses mitochondrial transcripts (Kim et al., 2018; Lee et al., 2020). Moreover, the transient associations between mRuby-PKR clusters and the ER align with recent findings showing that membrane-less organelles contact the ER (Lee et al., 2020).

Last, we asked whether PKR clustering is regulated by RNA binding. To this end, we used a pharmacogenetics approach in which we replaced PKR's RBDs with a "bump-and-hole" mutant (F36V) of the FKBP binding protein, which dimerizes with the synthetic bivalent ligand AP20187 (Clackson et al., 1998; Yang et al., 2000) (Fig. 3A). As expected, treating cells expressing FKBP-PKR with the dimerizer led to FKBP-PKR and eIF2α phosphorylation, protein synthesis shutdown, and induction of canonical ISR markers, including ATF4 and CHOP (Fig. 3B-E; S3A). Unexpectedly, FKBP-PKR also formed clusters in cells (Fig. 3F), which is consistent with a recent report indicating that PKR's kinase domains have front-to-front in addition to back-to-back interfaces (Mayo et al., 2019). FKBP-PKR clusters formed after 5 minutes of dimerizer treatment (Fig. 3F), and they were smaller than mRuby-PKR clusters, averaging 0.12 µm in diameter. Unlike the more persistent mRuby-PKR clusters, FKBP-PKR clusters completely dissolved 60 minutes after addition of the dimerizer (Fig. 3F, G), suggesting that PKR's RBDs and RNA binding are required to stabilize the clusters. Despite these differences, FKBP-PKR clusters colocalized with PBs (Fig. S3B), as occurred with some mRuby-PKR clusters (Fig. 2B; S2A, B). Taken together, these results indicate that ligand binding—RNA or dimerizer for PKR and FKBP-PKR, respectively—is required to nucleate the clusters.

eIF2α is not recruited to PKR clusters

Besides itself, PKR's best-characterized substrate is eIF2α (Thomis and Samuel, 1993; Dey et al., 2005). PKR interacts with eIF2α through the C-terminal catalytic lobe of its kinase domain (Dar et al., 2005). In an active PKR dimer, these catalytic lobes face away from the back-to-back dimer-forming interfaces between the kinase domains, which allows each PKR protomer to interact with eIF2α in a 1:1 stoichiometric ratio (Dar et al., 2005). Our observation that PKR clusters are composed of static and mobile fractions (Fig.1I) alludes that PKR clusters may limit the accessibility of eIF2α to active PKR pools. To investigate whether eIF2α enters PKR clusters, we conducted live-cell imaging analyses in H4 cells that co-express mRuby-PKR and eIF2α fused to the green fluorescent protein mNeon. To our surprise, we found that mNeon-eIF2α was diffuse in

the cytosol and not enriched in mRuby-PKR clusters in cells treated with poly I:C (Fig. 4A; Video 6;). Immunofluorescence analyses using a Ser51 phospho-eIF2α antibody in mRuby-PKR expressing cells treated with poly I:C corroborated showed phospho-eIF2α decorating the periphery of the clusters, which corroborated our findings (Fig. 4B). As expected, poly I:C treatment significantly increased the levels of phospho-eIF2α levels indicating activation of the ISR (Fig. 4B, C).

Because eIF2α is part of a trimeric complex composed of eIF2α, β, and γ subunits with a combined mass of ~125 kDa (Beilsten-Edmands et al., 2015; Llácer et al., 2015), it is possible that steric effects preclude accommodation into the active site of each PKR molecule in the cluster. To test whether this is the case, we generated a stable cell line co-expressing mRuby-PKR and the vaccinia virus eIF2α homolog K3L fused to mNeon. K3L is a small 88 amino acid protein that mimics the N-terminus of eIF2α and does not bind eIF2β and eIF2γ (Davies et al., 1992; Dar and Sicheri, 2002). Thus, we reasoned that this small PKR pseudosubstrate would not encounter the potential steric hindrance of eIF2. Indeed, we found that mNeon-K3L could access mRuby-PKR clusters, albeit with a lag time of about 10 minutes after their formation (Fig. 4D; Video 7). Taken together, these findings suggest that PKR clusters are not sites of eIF2α phosphorylation, but rather that they act as enzyme sinks that regulate the extent of eIF2α phosphorylation by limiting enzyme-substrate encounters.

PKR cluster disruption accelerates and enhances eIF2α phosphorylation

To test the hypothesis that PKR clusters regulate eIF2α phosphorylation, we introduced mutations in PKR to disable clustering *in vivo*. We focused on two residues (S462 and G466) in PKR's kinase domain that have been recently shown to be required to stabilize front-to-front PKR kinase-domain interfaces *in vitro* (Mayo et *al.,* 2019). We generated a stable H4 cell line expressing mRuby-PKR$^{S462A/G466L}$ in the background of CRISPRi-generated PKR depletion and tested the ability of this mRuby-PKR mutant to cluster upon poly I:C stimulation (Fig. 5A). As expected, live-cell imaging analyses showed that

the clustering ability of mRuby-PKR$^{S462A/G466L}$ was dramatically reduced (Fig. 5B, S5A; Video 8).

Surprisingly, and in contrast to what has been reported *in vitro* (Mayo et al., 2019), disruption of *in vivo* PKR clustering did not suppress PKR's self-phosphorylation but rather enhanced it (Fig. 5G, S5C). Moreover, mRuby-PKR$^{S462A/G466L}$ expressing cells exposed to poly I:C showed accelerated and enhanced eIF2α phosphorylation when compared to cells expressing mRuby-PKR, even though the levels of mRuby-PKR$^{S462A/G466L}$ were lower than those of mRuby-PKR (Fig. S5B). We observed similar results in cells expressing FKBP-PKR and FKBP-PKR$^{S462A/G466L}$ in which we activated signaling using the small molecule dimerizer (Fig. 5E-H). These results indicate that the front-to-front interfaces in PKR's kinase domain promote cluster formation and that PKR clusters limit substrate recruitment.

Discussion

Here, we identified a novel feature of PKR signaling: dynamic PKR clustering attenuates eIF2α phosphorylation. We base our conclusion on several lines of evidence. First, using live cell imaging analyses, we show that mRuby-PKR reorganizes into visible clusters upon stimulation with synthetic, viral, and endogenous dsRNAs. Second, even though PKR clusters share components with PBs, we found that pharmacological and genetic ablation of PBs did not negatively impact PKR cluster assembly, indicating that clustering is an intrinsic property of PKR. Third, through mutagenesis analyses, we found that ligand-driven self-association and front-to-front PKR kinase interfaces are required for cluster assembly. Fourth, our data indicate that eIF2α is excluded from PKR clusters, and disruption of PKR clustering enhanced downstream signaling. Mechanistically, our data support a model in which the functional consequence of PKR clustering is to regulate enzyme-substrate interactions to control the timing and amplitude of signaling.

The current model for PKR activation proposes that RNA-binding drives dimerization and trans-autophosphorylation to initiate signaling (Lemaire et al., 2005; Dar et al., 2005). This model is remarkably similar to the ER-resident stress sensor kinases IRE1 and PERK, which are also activated by self-association and trans-autophosphorylation (Cui et al., 2011; Zhou et al., 2006; Carrara et al., 2015; Korennykh et al., 2009, 1). IRE1 and PERK form dynamic high-order oligomers, as does the pseudokinase RNase L, a key player in the antiviral response (Bertolotti et al., 2000; Han et al., 2012; Lee et al., 2008; Li et al., 2010; Korennykh et al., 2009; Carrara et al., 2015). We found that PKR exhibits the same tendency to form dynamic clusters upon activation. Moreover, the structural similarities between the kinase domains of the mammalian ISR sensors raise the possibility that clustering is pervasive amongst them (Taniuchi et al., 2016). These observations support the notion that stress sensor clustering may be a common organizing principle for signaling.

Our finding that PB RNA-binding proteins (RBPs) (e.g., Edc3, Dcp1a, 4E-T) are recruited to PKR clusters (Fig. 2F) indicates compositional heterogeneity. Notably, FKBP-PKR clusters recruit Edc3, which suggests that either the interlinker domain, the kinase domain, or both are required for interaction with PB components. In contrast to enduring mRuby-PKR clusters, FKBP-PKR clusters are short-lived (Fig. 3F-G), indicating that PKR's RBDs—and RNA binding—stabilize PKR clusters and could further contribute to fine-tuning PKR signaling. It is noteworthy that the dissolution of PBs with cycloheximide or upon genetic depletion of 4E-T does not influence the kinetics and efficiency of PKR cluster formation. In line with these findings, PKR clusters formed during mitosis, when PBs naturally dissolve (Yang et al., 2004), indicating that PBs are dispensable for PKR clustering. These observations substantiate that PKR clusters are autonomous entities capable of recruiting some PB components, potentially through a piggyback mechanism. Such a mechanism requires further investigations. Moreover, even though PKR has been found in SGs (Reineke and Lloyd, 2015), our analyses indicate that PKR clusters and SGs are distinct. PKR clusters neither colocalize with SGs (Fig. 2A) nor are they ablated by cycloheximide (Fig. 2D-E), which

prevents SG formation (Mollet et al., 2008), which further attests to their autonomous nature.

Besides clustering, subcellular partitioning may provide an additional regulatory layer to control the ISR. Indeed, PERK is an ER-localized transmembrane protein (Harding et al., 1999), GCN2 associates with ribosomal components (Harding et al., 2019), and HRI has been reported to act as a signaling relay for mitochondrial stress (Guo et al., 2020; Fessler et al., 2020). Likewise, PKR has been observed in the nucleus and in contact with the mitochondrial network (Kim et al., 2018; Jeffrey et al., 1995; Blalock et al., 2014), and Fig. S2.2B, Video 4). We also found that PKR clusters transiently associate with the ER (Fig. S2.2B, Video 5), which raises the possibility that reshuffling PKR to different subcellular locales may regulate its access to local pools of eIF2. As a corollary, it is tempting to speculate that clustering of each ISR kinase in different subcellular niches could potentially control unique outputs.

Our most intriguing observation is that eIF2α is excluded from PKR clusters (Fig. 4A,B Video 6). Spatial reorganization can increase reaction rates of enzymatic reactions by concentrating enzymes and substrates into coalescences (Kohnhorst et al., 2017; An et al., 2008; Kim et al., 2019; Sheu-Gruttadauria and MacRae, 2018). However, it is difficult to reconcile our observations with this concept of “enzymatic factories” since disruption of PKR clusters led to enhanced PKR auto-phosphorylation (Fig. 5G, S4F), coupled to accelerated and boosted eIF2α phosphorylation (Fig. 4F, S5C). One possible explanation for this observation is that PKR’s phosphatases can be recruited to the clusters to suppress excessive PKR signaling. Further experiments will be required to test this hypothesis.

Our results suggest that tight packing of active PKR dimers results in steric effects that preclude eIF2α from entering PKR clusters. Our observations with the small PKR pseudosubstrate K3L, which can access PKR clusters, lend support to this notion. Moreover, the approximately 10-minute lag-time we observed between PKR cluster formation and K3L recruitment (Fig. 4D, Video 7) suggests that cluster formation is not

necessarily coupled to eIF2α phosphorylation. Given that PKR clusters appear to be biophysically heterogeneous (i.e., composed of a pool of PKR molecules that readily exchanges with the cytosol and another one that does not, Fig. 1I), it is possible that active PKR dimers on the periphery of the cluster freely exchange with the cytosol to fine-tune enzyme-substrate interactions. A recent report indicate that IRE1 and its substrate, the XBP1 mRNA, do not meet in high-order assemblies in mammalian cells, but rather that the IRE1-driven splicing reaction occurs in diffuse ER locales (Gomez-Puerta et al., 2021), which is consistent with our observations that eIF2α does not accumulate in PKR clusters.

Based on the evidence collected, we propose a hierarchical PKR cluster assembly model (Fig. 6). In an initial step, ligand binding nucleates the formation of active back-to-back PKR dimers. This step is followed by the coalescence of active dimers into higher-order coalescences promoted by front-to-front interfaces in PKR's kinase domain. In a subsequent step, heterologous protein-protein and protein-RNA interactions further stabilize the cluster, for example, upon recruitment of additional RNAs and RBPs, as would occur when PKR clusters and PBs merge (Fig. 2B) or when PKR clusters decorate SGs (Fig. 2A). Our findings support the intriguing possibility that stress sensor clustering calibrates the ISR to ensure non-adaptive outputs do not supersede homeostatic ones, thereby safeguarding the integrity of cells and tissues.

Materials and methods

Plasmid construction and generation of stable cell lines

H4 neuroglioma cells stably expressing a catalytically-dead version of Cas9 (dCas9) fused to the KRAB transcriptional repressor domain were a kind gift of Martin Kampmann. PKR was depleted in H4-dCas9-KRAB cells using CRISPR interference (CRISPRi) as previously described (Gilbert et al., 2014). The sgRNA sequence was obtained from the human genome-scale CRISPRi library developed by the laboratory of Jonathan Weissman. mRuby-PKR was generated by in-fusion cloning of the PCR-

amplified coding sequence of mRuby into the human PKR expression construct pDAA-002. pDAA-002 encodes a C-terminal FLAG-tagged version of human PKR hosted in the retroviral expression vector pLPCX (Clontech) and was generated by cloning a PCR product (PCRP) encoding the PKR coding sequence obtained from HEK-293 cells cDNA. This PCRP was obtained using oligonucleotides containing a 5' HindIII site and a 3' FLAG-epitope coding sequence and a NotI site and was cloned into the cognate sites of pLPCX using standard molecular biology techniques. FKBP-PKR was generated by cloning a PCRP encoding residues 170-551 of PKR of human origin obtained using oligonucleotides containing a 5'-BamHI site and a 3' FLAG-epitope coding sequence and MfeI sites into the cognate sites of p1XDmrB-mCh-LRP6c (kind gift of Peter Walter). The resulting construct, pDAA-006, replaces the mCh-LRP6c coding sequences in p1XDmrB-mCh-LRP6c with the abovementioned PKR coding sequence. The FLAG-epitope tagged FKBP-PKR coding sequence was excised from pDAA-006 with XhoI and MfeI and subcloned into the XhoI and EcoRI sites of pLPCX-IRES-eGFP. pLPCX-IRES-eGFP was generated by cloning a fusion PCRP consisting of the encephalomyocarditis virus internal ribosomal entry site (EMCV-IRES) upstream of the eGFP coding sequence flanked by EcoRI and NotI sites into the cognate sites of pLPCX (Clontech). A DNA gene block encoding the vaccinia virus Wisconsin strain K3L fused to the C-terminus of mNeonGreen by a GSGS linker and hosted into the expression vector pTwist Lenti SFFV puro WPRE was obtained commercially (Twist Bioscience). eIF2α-mNeon was generated by in-fusion cloning of a PCRP encoding the mNeon coding sequence into the mouse eIF2α expression construct pDAA-026 to generate pDAA-025. pDAA-026 was generated by subcloning a DNA fragment encoding an N-terminus FLAG-tagged mouse eIF2α coding sequence flanked by BamHI and EcoRI sites into the BglII and EcoRI sites of pLPCX (Clontech) using standard molecular biology methods. The coding sequence of wild-type, FLAG-tagged eIF2α of mouse origin was obtained from a mammalian expression construct (Sidrauski et al., 2013). Point mutants of the PKR coding sequence were generated by site-directed mutagenesis of the corresponding expression constructs. The plasmid encoding GFP-Dcp1a was a kind gift of Gia Voeltz (Addgene plasmid #153972). The expression construct for ERmoxGFP was a kind gift of Erik Snapp (Addgene plasmid #68072). All

viral vectors were used to generate recombinant lenti- and retroviruses and transduce cells as previously described (Sidrauski et al., 2013). Pseudoclonal stable cell lines were generated by fluorescence-activated cell sorting, selecting for a narrow gate encompassing the population expressing the mid-point level based on signal intensity of the fluorescent reporters. This population typically comprised ~5% of the transductant population. Expression levels were maintained by treating the cells with puromycin (1 µg/mL). Whenever dark cell lines were generated, they were selected using puromycin (1 µg/mL).

Cell culture, transfection, and drug treatments

H4 cells were maintained in DMEM supplemented with 10% FBS, L-glutamine and penicillin/streptomycin at 37°C, 5% CO2 in a humidified incubator. Mixed molecular weight Poly I:C (Tocris) was used at a final concentration of 2 µg/ml and transfected with Lipofectamine 2000 (Invitrogen) using the manufacturer's protocol. GFP-Dcp1a and ERmox-GFP transfections were carried out on 5×10^4 H4 cells in glass-bottom 24-well plates using 300 ng of DNA and Lipofectamine 2000 in a 1:2 ratio. Live-imaging analysis was performed 30 hours after transfection. Mitotracker green (Invitrogen) was diluted in serum free media (OPTI-Mem; Invitrogen) at a final concentration of 200 nM and was incubated for 30 minutes at 37°C before poly I:C transfection and imaging. Analysis of mRuby-PKR localization during the cell cycle was performed after synchronizing cells in G_1 with thymidine (Sigma-Aldrich). Briefly, 5×10^4 H4 cells were seeded in a glass-bottom 24-well plate and incubated overnight at 37°C. Cells were pulsed with thymidine (2 mM) for 18 hours and chased in complete media for 9 hours at 37°C. A second thymidine pulse was added before live-cell imaging. Cells were washed in in phenol-free complete media and images were acquired every 5 minutes for 16 hours. Mitotic events were observed ~8 hours of removal of thymidine. 1,6-hexanediol was diluted at a final concentration of 3.5% (v/v) in phenol red-free media and added directly to the cells. The AP20187 homodimerizer (Takara) was used at a final concentration of 100 nM for the indicated times. Sodium arsenite (Sigma Aldrich) was used at a final concentration of 500 µM for 1h. 4E-T gene silencing was obtained

through transfection of synthetic small interfering RNA (siRNA). Depletion of 4E-T was performed using a pool of synthetic small interfering RNAs (Dharmacon siGenome-SMART pool; 5'-UUACGAAUCACUGAGGUAGGG-3' and 5'-UCUCGUGGAUCUACUAUCCTG-3' and their reverse complements targeting gene NM_019843) transfected with Lipofectamine 2000 following the manufacturer's recommendations. All RNAi experiments were carried out at 96 h after transfection.

Measles virus infection

The measles virus C protein knockout (Moraten Vaccine strain MVvac-CKO-GFP) (Pfaller et al., 2014) was propagated in Vero cells at a multiplicity of infection (MOI) of 0.01. After 48 h, when cytopathic effect was visible in 100% of the culture, supernatants were collected, clarified by centrifugation at 350 × *g* for 5 minutes, and filtered through a 0.45 µm SFCA membrane. Aliquots of the viral stock were stored at -80 °C. The virus stock titer was determined by fluorescent focus assay on Vero cells. H4 cells expressing m-Ruby PKR were infected at an MOI of 0.5 for 48 hours and imaged by live-cell imaging confocal microscopy as described below.

Microscopy

Imaging was performed using an inverted spinning disc confocal microscope (Nikon Ti-Eclipse) equipped with an electron-multiplying charge-coupled device camera (Fusion, SN:500241) and environmental control (Okolabs stage top incubator). Live-cell imaging was performed at 37 °C and 5% CO_2. Images acquisition was performed with a 40 × NA 0.95 air objective. For fixed samples, a 100 × NA 1.49 oil immersion objective was used. Live-cell super-resolution Videos were acquired in a Nikon CSU-W1 SoRa spinning-disk confocal microscope equipped with an electron-multiplying charge-coupled device camera (Andor DU-888). Images were captured with a 60 × NA 1.2 water immersion objective.

FRAP analysis

FRAP analyses were carried out as previously described (Snapp et al., 2003) using a resonant scanning confocal microscope (Leica SP8). The mobile fraction was calculated as follows,

$$M_f = \frac{I_\infty - I_0}{I_i - I_0}$$

Where, I_∞ is the last fluorescence value collected, I_0 is the fluorescence value before photobleaching, and I_i is the first value after photobleaching. The immobile fraction was defined as 1 - M_f.

Immunofluorescence

0.8×10^5 H4 cells were grown on glass coverslips (Fisher Scientific) and fixed 24 hours after plating with 4% paraformaldehyde for 10 min or with ice-cold MeOH for 5 min. Fixed cells were washed with PBS, and permeabilized with blocking solution (0.05% saponin, 0.5% BSA, 50 mM, NH_4Cl in PBS) for 20 min. Afterwards, the samples were incubated 1 hr at RT with primary antibodies diluted in blocking solution at the concentrations specified in the table below. The coverslips were washed with three times with RT room-temperature PBS and incubated with fluorochrome-conjugated secondary antibodies (Alexa-Fluor-488, Alexa-Fluor-568 and Alexa-Fluor-647, diluted at 1:500 in blocking solution) and DAPI (0.1 µg/mL) for 45 min at RT. Cells were washed two times in PBS and one time in dd$H_2$0 before mounting using mowiol.

Antibody	Manufacturer	Cat. No.	Species	Dilution
ATF4	Cell Signaling Technology	11815	Rabbit	1:400
CHOP	Cell Signaling Technology	2895	Mouse	1:200
Edc3	Santa Cruz Biotechnology	271805	Mouse	1:600
FLAG	Sigma	F1804	Mouse	1:400
FLAG	Abcam	205606	Rabbit	1:400

GM130	DB laboratories	610822	Mouse	1:1000
G3BP1	Bethyl	A302-033A	Rabbit	1:1000
LAMP1	Cell Signaling Technology	9091	Rabbit	1:1500
LC3	Cell Signaling Technology	2775S	Rabbit	1:100
PMP70	Invitrogen	PA1-650	Rabbit	1:400
p-eIF2α	Abcam	ab32157	Rabbit	1:200
p-PKR	Abcam	ab32036	Rabbit	1:200
4E-T	Bethyl	A300-706A-M-2	Rabbit	1:400

Image quantification and analysis

Colocalization correlation analysis of Edc3 and mRuby-PKR was performed using the open-source image processing software Fiji (V2.3) as follows: A single-cell ROI was drawn manually for cells with mRuby-PKR clusters, and each cell crop was analyzed individually. After cropping, the image was split into single channels and the Edc3 signal was subtracted from the mRuby-PKR signal using the “image subtraction” plug-in, and the resulting image was used to estimate the diameter of Edc3-free mRuby-PKR clusters using the “analyze particles” plug-in and intermodes-automated thresholding. To quantify the extent of colocalization of mRuby-PKR and Edc3, the signal for mRuby-PKR clusters that are devoid of Edc3 was subtracted from the source image. The diameter of mRuby-PKR- and Edc3-positive clusters was estimated as described above. The number of cells containing mRuby-PKR and FKBP-PKR clusters was estimated using the “multi-point tool” plug-in. After normalizing “cells with clusters” to the “total number of cells” in the field-of-view (FOV), as determined by DAPI staining, we used the Fiji plugin “analyze particles”, to count PKR clusters. The area of the FKBP-PKR clusters was calculated using the same plugin. Fluorescent intensity profiles of the indicated ROI were obtained using the plugin “RGB profile plots” in ImageJ. GFP-Dcp1a and mRuby-PKR correlation over time in live-cell images was performed using the Fiji plugin EzColocalization (Stauffer et al., 2018). For each cell, the maximum correlation value over time was selected to plot the data. mRuby-PKR and mRuby-PKR$^{S462A/G466L}$ cluster analysis was performed using Cell Profiler 3.1.8 on at least 30 randomly chosen

FOVs for each experimental replicate. Briefly, the analysis pipeline works as follows: 1) Locate nuclei by global thresholding in the Hoechst channel. 2) Identify cells by adaptive Otsu thresholding propagating outwards from the previously identified nuclei. 3) Identify the cytoplasm by subtracting the "cell" signal from the "nucleus" signal. 4) Identify mRuby-PKR clusters by adaptive Otsu thresholding. 5) Measure object size and shape 6) Assign mRuby-PKR clusters to "parent" cells based on their spatial overlap with the previously identified ER masks. The data output from Cell Profiler was parsed and analyzed using Python 3.7.

Western blotting

Cells were washed three times with RT PBS and lysed in Laemmli sample buffer (30 mM Tris-HCl pH 6.8, 1%SDS, 10% (w/v) Glycerol, bromophenol blue). Lysates were briefly sonicated, 5% 2-mercaptoethanol was added, and the lysates were heated up top 95 °C prior to separation by SDS-PAGE. Immunoblotting was performed using nitrocellulose membranes blocked with 1% BSA in TBS-T for 45 minutes, and incubated at 4 °C overnight with the following antibodies: anti-PKR (1:1000; Cell Signaling cat. No. 3072), anti-p-PKR (1:1000; Sigma Aldrich cat. No. MA5-32-086 or 1:1000; Abcam cat. No. 32036), anti-p-eIF2α (1:1000; Cell signaling cat. No. 9721), anti-eIF2α (1:1000; Cell signaling cat. No. 9722), anti-ATF4 (1:1000; Cell signaling cat. No. 11815S), anti-CHOP (1:1000; Cell signaling cat. No. 2895S), anti-GADD34 (1:1000; Proteintech 10449-1-AP), anti-FLAG M2 (1:3000; Sigma F1804), anti-puromycin (1:2000; Millipore 2266S), anti-ß-actin (1:5000, Sigma Aldrich cat. No. 061M4808), anti-GAPDH (1:5000, Abcam cat. No. 8245). Membranes were washed three times with TBS-T buffer and incubated at RT for 1 hour with horseradish peroxidase-conjugated secondary anti-mouse or anti-rabbit antibodies (1:5000; Cell Signaling Technology). The membranes were washed three times in TBS-T, and immunoreactive bands were detected by enhanced chemiluminescence.

Puromycilation of nascent peptides

Puromycilation of nascent peptides was performed as described (Zappa et al., 2019). Briefly, 2×10^5 FKBP-PKR cells were grown in 6-well plates and the AP20187 homodimerizer was added 24 hours after. 9 µM puromycin (PMY) as wadded one hour after addition of AP20187. Cells were incubated with PMY for 20 min at 37°C before sample collection. The cells were collected and analyzed as described for Western blotting.

Immunoprecipitation

5×10^6 FKBP-PKR and FKBP- PKR$^{S462A/G466L}$ cells were washed three times in cold PBS and lysed in IP buffer (25mM Tris-HCl pH 7.4, 150mM NaCl, 1mM EDTA, 0.5% NP40, supplemented with fresh protease and phosphatase inhibitors). The lysates were clarified for 15 minutes at 10,000 $\times$ *g* at 4°C, and the clarified cell extracts were immunoprecipitated for 3 hours at 4 °C using FLAG-M2 magnetic beads with end-over-end rotation. The beads were washed 6 times in IP buffer and target antigens were recovered by incubating the beads in 100 mM Glycine pH 2.8 for 20 minutes at 4 °C. The eluates were immediately neutralized with 500 mM Tris pH 8.0 before separation by SDS-PAGE. Western blot analysis was performed as described above.

Figure legends

Figure 1. mRuby-PKR forms clusters in response to synthetic and natural inputs. A) Representative time-lapse micrographs showing discrete mRuby-PKR clusters in H4 cells transfected with poly I:C. Scale bar: 10 µm. B) Violin plots showing the maximum number of mRuby-PKR clusters per cell in H4 cells transfected with poly I:C (N = 5, n > 200 cells). C) Representative live imaging time-lapse showing merging and segregation of mRuby-PKR clusters. Scale bar 2 µm. D) Representative immunofluorescence image with a phospho-specific PKR antibody (T446) showing PKR is phosphorylated in the clusters. Scale bar: 10 µm. E) Representative micrograph showing formation of mRuby-PKR clusters in measles-infected (strain MVvac-CKO-GFP) H4 cells. The inset corresponds with the outlined cell in the high-magnification image. Note that the

uninfected cell in the top left corner shows no mRuby-PKR clusters. Scale bar: 10 µm. F) Quantification of *de novo* mRuby-PKR clustering frequency (red bars) and MVvac-CKO-GFP replication (GFP mean fluorescence intensity and 95% CI bands) as function of time. Red trace: non-linear curve fit of the mRuby-PKR clustering frequency data. The percentage of infected cells that formed mRuby-PKR clusters was, on average, 45% ± 5% (N = 3, n > 400 cells). G) Representative time-lapse micrographs showing the formation of mRuby-PKR clusters (yellow arrowheads) in dividing H4 cells. Scale bar: 10 µm H) Quantification of normalized mRuby-PKR cluster fluorescence intensity in 1,6-hexandiol treated H4 cells. T0 corresponds to 60 min of poly I:C treatment. The data were binned and are shown as the mean and 95% CI bands (n = 60 cells). The micrographs show representative images of mRuby-PKR cluster dissolution by 1,6-hexandiol treatment. Scale bar: 10 µm. I) FRAP analysis showing the recovery of normalized fluorescence intensity of mRuby-PKR clusters. The data are shown as in H (N = 3, n = 30 cells). The micrographs show representative images of a single mRuby-PKR cluster photobleached with a 561 nm laser beam.

Figure 2. PKR clusters are autonomous and recruit PB components. A) Representative immunofluorescence images showing that mRuby-PKR clusters and G3BP1, a SG component, do not colocalize. Right panel: Plot of signal intensity of mRuby-PKR clusters (red) or G3BP1 immunostaining (green) as a function of distance. The ROI used for metrics is indicated with a white line on the micrograph crops. Scale bars: 10 µm. B) Time-lapse micrographs showing colocalization and subsequent de-mixing of mRuby-PKR and GFP-Dcp1a, a PB component. Scale bar: 10 µm. C) Quantification of the data in panel B (mean and 95% CI bands, N = 3, n = 30 cells). D) Violin plots showing the total number of cells with mRuby-PKR clusters after administration of poly I:C (blue), poly I:C and CHX (red), and poly I:C and 4E-T RNAi (green); N = 3, n > 2000; ns: not significant (One-way ANOVA). E) Violin plots showing the number of mRuby-PKR clusters per cell over time in cells treated with poly I:C (blue), poly I:C and CHX (red), and poly I:C and 4E-T RNAi (green). N = 3, n > 200. F) Representative micrographs showing that mRuby-PKR clusters recruit the PB component Edc3 after depletion of PBs with CHX and 4E-T RNAi. Scale bar: 10 µm.

Figure 3. PKR cluster formation requires ligand binding to PKR's sensor domain. A) Schematic representation of the pharmacogenetic approach for PKR activation using a synthetic dimerizer ligand. B) Western blots showing forced-dimerization of PKR results in phosphorylation of eIF2α. Right panel: quantification of the extent of eIF2α phosphorylation (mean and SEM, N = 3). C) Western blot showing forced-dimerization of PKR results in global protein synthesis shutdown as assessed by abundance of puromycilated peptides. D) Representative micrographs showing that forced-dimerization of PKR results in accumulation of ATF4 and CHOP. Tg, 24: thapsigargin treatment (300 nM, 24h; positive control). E) Western blots showing forced-dimerization of PKR results in induction of canonical ISR target genes. ß-actin, GAPDH: loading controls. The right panels show the quantification of the data (mean and SEM, N = 3). F) Representative micrograph showing that forced dimerization of PKR results in formation of PKR clusters. Scale bar: 10 µm. G) Quantification of the data in panel F (mean and SEM). N = 3, n > 500.

Figure 4. eIF2α does not accumulate in PKR clusters. A) Representative time-lapse images of cells co-expressing mRuby-PKR and mNeon-eIF2α showing that mNeon-eIF2α does not accumulate in mRuby-PKR clusters in response to poly I:C treatment. B) Representative immunofluorescence images showing phosphorylated eIF2α is excluded from PKR clusters. The micrograph crops on the right show that phosphorylated eIF2α decorates the periphery of mRuby-PKR clusters. Scale bar: 10 µm. C) Quantification of the mean fluorescence intensity of the phosphorylated eIF2α signal in immunofluorescence analyses (mean fold change and SEM, N = 3). SA: sodium arsenite; positive control. D) Representative time-lapse images showing that the fluorescently-labelled PKR pseudosubstrate mNeon-K3L enters mRuby-PKR clusters. Note the ~10 minute time-lag between formation of mRuby-PKR clusters and recruitment of mNeon-K3L to them. Scale bar: 10 µm.

Figure 5. PKR cluster disruption accelerates and enhances eIF2α phosphorylation. A) Schematic representation showing the mutations that disrupt

PKR's front-to-front (FTF) kinase interfaces. B) Quantification of imaging data showing that the mutations in PKR's FTF kinase interfaces severely reduce PKR clusters in cells. Cells with less than 3 or more that 50 clusters were not considered in this analysis. The data were binned and are shown as the mean and 95% CI bands, n > 2000. C) Western blots showing that cluster-disrupting mutations in PKR accelerate and enhance eIF2α phosphorylation in response to poly I:C treatment. D) Quantification of the data in C (mean and SEM, N = 3), P < 0.0001 (One-way ANOVA). D) Representative immunofluorescence images showing that the mutations in PKR's FTF kinase interfaces impair PKR cluster formation upon forced PKR activation with a synthetic dimerizer. Scale bar: 10 µm. E) Quantification of the data in D. E) Western blots showing accelerated and enhanced PKR autophosphorylation and phosphorylation of eIF2α in cells expressing FKBP-PKR upon mutation of PKR's FTF interfaces. F) Quantification of the data in E (mean and SEM, N = 2). P < 0.05, Student's t-test. Note that the augmented eIF2α phosphorylation is lost after 15 minutes, which is consistent with the time of dissolution of FKBP-PKR clusters (See Fig. 3G).

Figure 6. Model for the assembly of PKR clusters and their role in fine-tuning signaling. PKR is monomeric when inactive. dsRNA binding to its sensor domain drives dimerization and cluster assembly alongside PB components. The newly-minted PKR clusters act as enzyme sinks that attenuate eIF2α phosphorylation whereas active PKR dimers that exchange with the clusters drive eIF2α phosphorylation.

Supplementary Figure 1. Generation of a stable cell line expressing fluorescently-tagged PKR. A) Schematic representation of the expression construct encoding mRuby- and FLAG-tagged PKR of human origin. The mRuby fluorescent protein (236 aa) was inserted between residues 221 and 222 of human PKR. B) Western blot showing the level of expression of mRuby-PKR compared that of endogenous PKR. The relative protein amount determined by densitometry is shown below the blots. Endogenous PKR was depleted using CRISPRi. GAPDH: loading control. C) Representative micrograph showing that mRuby-PKR is a cytosolic soluble protein. Scale bar: 10 µm. D) Violin plots showing the diameter of mRuby-PKR clusters in H4

cells stably expressing mRuby-PKR and treated with poly I:C. E) Quantification of the half-life of mRuby-PKR in clusters after photobleaching. E) Quantification of the mRuby-PKR immobile fraction in clusters after photobleaching. For E and F; N = 3, n = 30 cells.

Supplementary Figure 2.1. Analysis of interdependence and colocalization of mRuby-PKR and PBs. A) Representative immunofluorescence images showing two populations of mRuby-PKR clusters based on their diameter and association with Edc3. The image crop shows a close-up of these two populations. Scale bar: 10 µm. The right panel shows the quantification of the data (n = 30 cells). B) Representative micrographs of fixed cells co-expressing mRuby-PKR and GFP-Dcp1a. The image crop shows two mRuby-PKR cluster populations; those that associate with GFP-Dcp1a and those that do not. Scale bar: 10 µm. C) Representative immunofluorescence images showing pharmacological (CHX) or genetic (4E-T RNAi) knock-down of PBs assessed by Edc3 staining. Scale bar: 10 µm. D) Representative micrographs showing that mRuby-PKR clusters recruit 4E-T after pharmacologic depletion (CHX) of PBs. Scale bar: 10 µm. E) Western blot showing the extent of knock-down of 4E-T KD by RNAi. Right panel: quantification of the data (mean and SEM, N = 3). $P < 0.0001$.

Supplementary Figure 2.2. Colocalization analysis of mRuby-PKR with membrane-bound organelles. A) Representative immunofluorescence images showing that mRuby-PKR clusters do not colocalize with the autophagosomes (LC3), lysosomes (LAMP1), early endosomes (EEA1), peroxisomes (PMP-70), or the cis-medial Golgi apparatus (GM130). The plots of signal intensity of mRuby-PKR clusters (red) and organelle markers (green) as a function of distance were prepared as in Fig. 2A. The ROIs used for metrics are indicated with a white line. Scale bar: 10 µm. B) Representative time-lapse micrographs showing transient association of mRuby-PKR clusters with mitochondria (mitotracker) or the ER (ERmox-GFP). Scale bar: 10 µm; inset: 2µm.

Supplementary Figure 3. RNA-independent activation of PKR triggers clustering and induces the ISR. A) Quantitative real-time PCR analysis of GADD34 and CHOP

levels after forced-dimerization of PKR with a synthetic ligand (mean and SEM, N = 5). B) Representative immunofluorescence images showing colocalization of FLAG-tagged FKBP-PKR and Edc3. Image crop on right: close-up. Scale bar: 10 µm.

Supplementary Figure 5. Suppression of PKR clustering enhances signaling. A) Image quantification showing that the mutations in PKR's FTF kinase interfaces significantly reduce the number of PKR clusters in cells. The data were binned and are shown as the mean and 95% Cl bands (n = 2000 cells). C) Flow cytometry histograms showing the relative fluorescent intensity of cells expressing wild-type mRuby-PKR (blue trace) and FTF mutant mRuby-PKR (red trace). D) Western blots showing the extent of FKBP-PKR's autophosphorylation after forced dimerization with a synthetic ligand for 1 h. Note that the phospho-PKR antibody also recognizes the unphosphorylated species (see Fig. 3B).

Video captions

Video 1. mRuby-PKR forms clusters in response to poly I:C treatment. The squares indicate areas of cluster merging (bottom right) and segregation (upper left).

Video 2. mRuby-PKR forms clusters during cell division.

Video 3. mRuby-PKR clusters and PBs (GFP-Dcp1a) de-mix in a time-dependent manner.

Video 4. mRuby-PKR forms transient associations with mitochondria (mitotracker green).

Video 5. mRuby-PKR forms transient associations with the ER (ERmox-GFP).

Video 6. mRuby-PKR clusters do not recruit mNeon-eIF2α.

Video 7. mRuby-PKR clusters recruit mNeon-K3L.

Video 8. Disruption of PKR's kinase FTF interfaces suppresses clustering.

Acknowledgements

We are grateful to Dzwokai Zach Ma and Charles E Samuel for their kind gift of the measles virus protein C knockout mutant strain, Carolina Arias for assistance with the measles virus infections, Julien Bacal for help with data analyses in Cell Profiler, and Meghan Morrisey and Maxwell Z. Wilson for providing us with access to their microscopy set-ups. We also thank Michael Costello and the members of the Acosta-Alvear and Arias labs for insightful discussion. This work as supported by a sponsored research agreement with Calico Life Sciences LLC (D.A-A.), a UCSB Academic Senate Faculty Research grant (D.A-A.), Departmental start-up funds (D.A-A.), and an Otis Williams Postdoctoral Fellowship (F.Z.).

Author contributions

D.A-A. supervised the research. F.Z. and D.A-A. designed the experiments, analyzed the data, and wrote the manuscript. N.L.M. generated the stable cell lines. J.C.P-R. produced the constructs used in the study.

Author disclosures

D.A-A. is an inventor on U.S. patent 9708247 held by the Regents of the University of California that describes ISRIB and its analogs. Rights to the invention have been licensed to Calico Life Sciences LLC. For the rest of the authors there are no competing interests.

Bibliography

Alberti, S., A. Gladfelter, and T. Mittag. 2019. Considerations and Challenges in Studying Liquid-Liquid Phase Separation and Biomolecular Condensates. *Cell*. 176:419–434. doi:10.1016/j.cell.2018.12.035.

An, S., R. Kumar, E.D. Sheets, and S.J. Benkovic. 2008. Reversible Compartmentalization of de Novo Purine Biosynthetic Complexes in Living Cells. *Science*. 320:103–106. doi:10.1126/science.1152241.

Andrei, M.A., D. Ingelfinger, R. Heintzmann, T. Achsel, R. Rivera-Pomar, and R. Lührmann. 2005. A role for eIF4E and eIF4E-transporter in targeting mRNPs to mammalian processing bodies. *RNA*. 11:717–727. doi:10.1261/rna.2340405.

Balachandran, S., P.C. Roberts, L.E. Brown, H. Truong, A.K. Pattnaik, D.R. Archer, and G.N. Barber. 2000. Essential Role for the dsRNA-Dependent Protein Kinase PKR in Innate Immunity to Viral Infection. *Immunity*. 13:129–141. doi:10.1016/S1074-7613(00)00014-5.

Bando, Y., R. Onuki, T. Katayama, T. Manabe, T. Kudo, K. Taira, and M. Tohyama. 2005. Double-strand RNA dependent protein kinase (PKR) is involved in the extrastriatal degeneration in Parkinson's disease and Huntington's disease. *Neurochem Int*. 46:11–18. doi:10.1016/j.neuint.2004.07.005.

Beilsten-Edmands, V., Y. Gordiyenko, J.C. Kung, S. Mohammed, C. Schmidt, and C.V. Robinson. 2015. eIF2 interactions with initiator tRNA and eIF2B are regulated by post-translational modifications and conformational dynamics. *Cell Discov*. 1:15020. doi:10.1038/celldisc.2015.20.

Belyy, V., I. Zuazo-Gaztelu, A. Alamban, A. Ashkenazi, and P. Walter. 2021. Endoplasmic reticulum stress activates human IRE1α through reversible assembly of inactive dimers into small oligomers. Biophysics.

Ben-Asouli, Y., Y. Banai, Y. Pel-Or, A. Shir, and R. Kaempfer. 2002. Human interferon-gamma mRNA autoregulates its translation through a pseudoknot that activates the interferon-inducible protein kinase PKR. *Cell*. 108:221–232. doi:10.1016/s0092-8674(02)00616-5.

Bertolotti, A., Y. Zhang, L.M. Hendershot, H.P. Harding, and D. Ron. 2000. Dynamic interaction of BiP and ER stress transducers in the unfolded-protein response. *Nat Cell Biol*. 2:326–332. doi:10.1038/35014014.

Blalock, W.L., M. Piazzi, A. Bavelloni, M. Raffini, I. Faenza, A. D'Angelo, and L. Cocco. 2014. Identification of the PKR nuclear interactome reveals roles in ribosome biogenesis, mRNA processing and cell division. *J Cell Physiol*. 229:1047–1060. doi:10.1002/jcp.24529.

Carrara, M., F. Prischi, P.R. Nowak, and M.M. Ali. 2015. Crystal structures reveal transient PERK luminal domain tetramerization in endoplasmic reticulum stress signaling. *EMBO J*. 34:1589–1600. doi:10.15252/embj.201489183.

Chung, H., J.J.A. Calis, X. Wu, T. Sun, Y. Yu, S.L. Sarbanes, V.L. Dao Thi, A.R. Shilvock, H.-H. Hoffmann, B.R. Rosenberg, and C.M. Rice. 2018. Human ADAR1 Prevents Endogenous RNA from Triggering Translational Shutdown. *Cell*. 172:811-824.e14. doi:10.1016/j.cell.2017.12.038.

Clackson, T., W. Yang, L.W. Rozamus, M. Hatada, J.F. Amara, C.T. Rollins, L.F. Stevenson, S.R. Magari, S.A. Wood, N.L. Courage, X. Lu, F. Cerasoli, M. Gilman, and D.A. Holt. 1998. Redesigning an FKBP-ligand interface to generate chemical dimerizers with novel specificity. *Proceedings of the National Academy of Sciences*. 95:10437–10442. doi:10.1073/pnas.95.18.10437.

Cole, J.L. 2007. Activation of PKR: an open and shut case? *Trends Biochem Sci*. 32:57–62. doi:10.1016/j.tibs.2006.12.003.

Costa-Mattioli, M., and P. Walter. 2020. The integrated stress response: From mechanism to disease. *Science*. 368:eaat5314. doi:10.1126/science.aat5314.

Cougot, N., S. Babajko, and B. Séraphin. 2004. Cytoplasmic foci are sites of mRNA decay in human cells. *Journal of Cell Biology*. 165:31–40. doi:10.1083/jcb.200309008.

Cui, W., J. Li, D. Ron, and B. Sha. 2011. The structure of the PERK kinase domain suggests the mechanism for its activation. *Acta Crystallogr D Biol Crystallogr*. 67:423–428. doi:10.1107/S0907444911006445.

Dar, A.C., T.E. Dever, and F. Sicheri. 2005. Higher-Order Substrate Recognition of eIF2α by the RNA-Dependent Protein Kinase PKR. *Cell*. 122:887–900. doi:10.1016/j.cell.2005.06.044.

Dar, A.C., and F. Sicheri. 2002. X-Ray Crystal Structure and Functional Analysis of Vaccinia Virus K3L Reveals Molecular Determinants for PKR Subversion and Substrate Recognition. *Molecular Cell*. 10:295–305. doi:10.1016/S1097-2765(02)00590-7.

Davies, M.V., O. Elroy-Stein, R. Jagus, B. Moss, and R.J. Kaufman. 1992. The vaccinia virus K3L gene product potentiates translation by inhibiting double-stranded-RNA-activated protein kinase and phosphorylation of the alpha subunit of eukaryotic initiation factor 2. *J Virol*. 66:1943–1950. doi:10.1128/JVI.66.4.1943-1950.1992.

Dey, M., C. Cao, A.C. Dar, T. Tamura, K. Ozato, F. Sicheri, and T.E. Dever. 2005. Mechanistic Link between PKR Dimerization, Autophosphorylation, and eIF2α Substrate Recognition. *Cell*. 122:901–913. doi:10.1016/j.cell.2005.06.041.

Dougherty, J.D., L.C. Reineke, and R.E. Lloyd. 2014. mRNA Decapping Enzyme 1a (Dcp1a)-induced Translational Arrest through Protein Kinase R (PKR) Activation Requires the N-terminal Enabled Vasodilator-stimulated Protein Homology 1

(EVH1) Domain *. *Journal of Biological Chemistry*. 289:3936–3949. doi:10.1074/jbc.M113.518191.

Elbarbary, R.A., W. Li, B. Tian, and L.E. Maquat. 2013. STAU1 binding 3′ UTR IRAlus complements nuclear retention to protect cells from PKR-mediated translational shutdown. *Genes Dev.* 27:1495–1510. doi:10.1101/gad.220962.113.

Fare, C.M., A. Villani, L.E. Drake, and J. Shorter. 2021. Higher-order organization of biomolecular condensates. *Open Biol.* 11:210137. doi:10.1098/rsob.210137.

Fessler, E., E.-M. Eckl, S. Schmitt, I.A. Mancilla, M.F. Meyer-Bender, M. Hanf, J. Philippou-Massier, S. Krebs, H. Zischka, and L.T. Jae. 2020. A pathway coordinated by DELE1 relays mitochondrial stress to the cytosol. *Nature*. 579:433–437. doi:10.1038/s41586-020-2076-4.

García, M.A., E.F. Meurs, and M. Esteban. 2007. The dsRNA protein kinase PKR: Virus and cell control. *Biochimie*. 89:799–811. doi:10.1016/j.biochi.2007.03.001.

Gilbert, L.A., M.A. Horlbeck, B. Adamson, J.E. Villalta, Y. Chen, E.H. Whitehead, C. Guimaraes, B. Panning, H.L. Ploegh, M.C. Bassik, L.S. Qi, M. Kampmann, and J.S. Weissman. 2014. Genome-Scale CRISPR-Mediated Control of Gene Repression and Activation. *Cell*. 159:647–661. doi:10.1016/j.cell.2014.09.029.

Gomez-Puerta, S., R. Ferrero, T. Hochstoeger, I. Zubiri, J.A. Chao, T. Aragon, and F. Voigt. 2021. Live imaging of the co-translational recruitment of XBP1 mRNA to the ER and its processing by diffuse, non-polarized IRE1a. Cell Biology.

Guo, X., G. Aviles, Y. Liu, R. Tian, B.A. Unger, Y.-H.T. Lin, A.P. Wiita, K. Xu, M.A. Correia, and M. Kampmann. 2020. Mitochondrial stress is relayed to the cytosol by an OMA1-DELE1-HRI pathway. *Nature*. 579:427–432. doi:10.1038/s41586-020-2078-2.

Han, Y., G. Whitney, J. Donovan, and A. Korennykh. 2012. Innate Immune Messenger 2-5A Tethers Human RNase L into Active High-Order Complexes. *Cell Reports*. 2:902–913. doi:10.1016/j.celrep.2012.09.004.

Harding, H.P., A. Ordonez, F. Allen, L. Parts, A.J. Inglis, R.L. Williams, and D. Ron. 2019. The ribosomal P-stalk couples amino acid starvation to GCN2 activation in mammalian cells. *eLife*. 8:e50149. doi:10.7554/eLife.50149.

Harding, H.P., Y. Zhang, and D. Ron. 1999. Protein translation and folding are coupled by an endoplasmic-reticulum-resident kinase. *Nature*. 397:271–274. doi:10.1038/16729.

Hebner, C.M., R. Wilson, J. Rader, M. Bidder, and L.A. Laimins. 2006. Human papillomaviruses target the double-stranded RNA protein kinase pathway. *J Gen Virol*. 87:3183–3193. doi:10.1099/vir.0.82098-0.

Hugon, J., F. Mouton-Liger, J. Dumurgier, and C. Paquet. 2017. PKR involvement in Alzheimer's disease. *Alz Res Therapy*. 9:83. doi:10.1186/s13195-017-0308-0.

Jeffrey, I.W., S. Kadereit, E.F. Meurs, T. Metzger, M. Bachmann, M. Schwemmle, A.G. Hovanessian, and M.J. Clemens. 1995. Nuclear localization of the interferon-inducible protein kinase PKR in human cells and transfected mouse cells. *Exp Cell Res*. 218:17–27. doi:10.1006/excr.1995.1126.

Kim, S., K. Lee, Y.S. Choi, J. Ku, Y.J. Lee, and Y. Kim. 2020. Mitochondrial dsRNAs activate PKR and TLR3 to promote chondrocyte degeneration in osteoarthritis.

Kim, T.H., B. Tsang, R.M. Vernon, N. Sonenberg, L.E. Kay, and J.D. Forman-Kay. 2019. Phospho-dependent phase separation of FMRP and CAPRIN1 recapitulates regulation of translation and deadenylation. *Science*. 365:825–829. doi:10.1126/science.aax4240.

Kim, Y., J.H. Lee, J.-E. Park, J. Cho, H. Yi, and V.N. Kim. 2014. PKR is activated by cellular dsRNAs during mitosis and acts as a mitotic regulator. *Genes Dev.* 28:1310–1322. doi:10.1101/gad.242644.114.

Kim, Y., J. Park, S. Kim, M. Kim, M.-G. Kang, C. Kwak, M. Kang, B. Kim, H.-W. Rhee, and V.N. Kim. 2018a. PKR Senses Nuclear and Mitochondrial Signals by Interacting with Endogenous Double-Stranded RNAs. *Molecular Cell*. 71:1051-1063.e6. doi:10.1016/j.molcel.2018.07.029.

Kim, Y., J. Park, S. Kim, M. Kim, M.-G. Kang, C. Kwak, M. Kang, B. Kim, H.-W. Rhee, and V.N. Kim. 2018b. PKR Senses Nuclear and Mitochondrial Signals by Interacting with Endogenous Double-Stranded RNAs. *Mol Cell*. 71:1051-1063.e6. doi:10.1016/j.molcel.2018.07.029.

Kohnhorst, C.L., M. Kyoung, M. Jeon, D.L. Schmitt, E.L. Kennedy, J. Ramirez, S.M. Bracey, B.T. Luu, S.J. Russell, and S. An. 2017. Identification of a multienzyme complex for glucose metabolism in living cells. *J Biol Chem*. 292:9191–9203. doi:10.1074/jbc.M117.783050.

Korennykh, A.V., P.F. Egea, A.A. Korostelev, J. Finer-Moore, C. Zhang, K.M. Shokat, R.M. Stroud, and P. Walter. 2009. The unfolded protein response signals through high-order assembly of Ire1. *Nature*. 457:687–693. doi:10.1038/nature07661.

Kroschwald, S., S. Maharana, D. Mateju, L. Malinovska, E. Nüske, I. Poser, D. Richter, and S. Alberti. 2015. Promiscuous interactions and protein disaggregases determine the material state of stress-inducible RNP granules. *eLife*. 4:e06807. doi:10.7554/eLife.06807.

Lavoie, H., J.J. Li, N. Thevakumaran, M. Therrien, and F. Sicheri. 2014. Dimerization-induced allostery in protein kinase regulation. *Trends in Biochemical Sciences*. 39:475–486. doi:10.1016/j.tibs.2014.08.004.

Lee, H., R.J. Fenster, S.S. Pineda, W.S. Gibbs, S. Mohammadi, J. Davila-Velderrain, F.J. Garcia, M. Therrien, H.S. Novis, F. Gao, H. Wilkinson, T. Vogt, M. Kellis, M.J. LaVoie, and M. Heiman. 2020a. Cell Type-Specific Transcriptomics Reveals that Mutant Huntingtin Leads to Mitochondrial RNA Release and Neuronal Innate Immune Activation. *Neuron*. 107:891-908.e8. doi:10.1016/j.neuron.2020.06.021.

Lee, J.E., P.I. Cathey, H. Wu, R. Parker, and G.K. Voeltz. 2020b. Endoplasmic reticulum contact sites regulate the dynamics of membraneless organelles. *Science*. 367:eaay7108. doi:10.1126/science.aay7108.

Lee, K.P.K., M. Dey, D. Neculai, C. Cao, T.E. Dever, and F. Sicheri. 2008. Structure of the dual enzyme Ire1 reveals the basis for catalysis and regulation in nonconventional RNA splicing. *Cell*. 132:89–100. doi:10.1016/j.cell.2007.10.057.

Lemaire, P.A., J. Lary, and J.L. Cole. 2005. Mechanism of PKR activation: dimerization and kinase activation in the absence of double-stranded RNA. *J Mol Biol*. 345:81–90. doi:10.1016/j.jmb.2004.10.031.

Li, H., A.V. Korennykh, S.L. Behrman, and P. Walter. 2010. Mammalian endoplasmic reticulum stress sensor IRE1 signals by dynamic clustering. *Proc Natl Acad Sci U S A*. 107:16113–16118. doi:10.1073/pnas.1010580107.

Llácer, J.L., T. Hussain, L. Marler, C.E. Aitken, A. Thakur, J.R. Lorsch, A.G. Hinnebusch, and V. Ramakrishnan. 2015. Conformational Differences between Open and Closed States of the Eukaryotic Translation Initiation Complex. *Mol Cell*. 59:399–412. doi:10.1016/j.molcel.2015.06.033.

Luo, Y., Z. Na, and S.A. Slavoff. 2018. P-Bodies: Composition, Properties, and Functions. *Biochemistry*. 57:2424–2431. doi:10.1021/acs.biochem.7b01162.

Maia de Oliveira, T., V. Korboukh, S. Caswell, J.J. Winter Holt, M. Lamb, A.W. Hird, and R. Overman. 2020. The structure of human GCN2 reveals a parallel, back-to-back kinase dimer with a plastic DFG activation loop motif. *Biochem J*. 477:275–284. doi:10.1042/BCJ20190196.

Martinez, N.W., F.E. Gómez, and S. Matus. 2021. The Potential Role of Protein Kinase R as a Regulator of Age-Related Neurodegeneration. *Front Aging Neurosci*. 13:638208. doi:10.3389/fnagi.2021.638208.

Mayo, C.B., H. Erlandsen, D.J. Mouser, A.G. Feinstein, V.L. Robinson, E.R. May, and J.L. Cole. 2019. Structural Basis of Protein Kinase R Autophosphorylation. *Biochemistry*. 58:2967–2977. doi:10.1021/acs.biochem.9b00161.

Mollet, S., N. Cougot, A. Wilczynska, F. Dautry, M. Kress, E. Bertrand, and D. Weil. 2008. Translationally Repressed mRNA Transiently Cycles through Stress Granules during Stress. *Mol Biol Cell*. 19:4469–4479. doi:10.1091/mbc.E08-05-0499.

Okonski, K.M., and C.E. Samuel. 2013. Stress Granule Formation Induced by Measles Virus Is Protein Kinase PKR Dependent and Impaired by RNA Adenosine Deaminase ADAR1. *J Virol*. 87:756–766. doi:10.1128/JVI.02270-12.

Peel, A.L. 2001. Double-stranded RNA-dependent protein kinase, PKR, binds preferentially to Huntington's disease (HD) transcripts and is activated in HD tissue. *Human Molecular Genetics*. 10:1531–1538. doi:10.1093/hmg/10.15.1531.

Pfaller, C.K., M.J. Radeke, R. Cattaneo, and C.E. Samuel. 2014. Measles virus C protein impairs production of defective copyback double-stranded viral RNA and activation of protein kinase R. *Journal of Virology*. 88:456–468. doi:10.1128/JVI.02572-13.

Pindel, A., and A. Sadler. 2011. The role of protein kinase R in the interferon response. *J Interferon Cytokine Res*. 31:59–70. doi:10.1089/jir.2010.0099.

Protter, D.S.W., and R. Parker. 2016. Principles and Properties of Stress Granules. *Trends in Cell Biology*. 26:668–679. doi:10.1016/j.tcb.2016.05.004.

Reineke, L.C., N. Kedersha, M.A. Langereis, F.J.M. van Kuppeveld, and R.E. Lloyd. 2015. Stress Granules Regulate Double-Stranded RNA-Dependent Protein Kinase Activation through a Complex Containing G3BP1 and Caprin1. *mBio*. 6:e02486-14. doi:10.1128/mBio.02486-14.

Reineke, L.C., and R.E. Lloyd. 2015. The stress granule protein G3BP1 recruits protein kinase R to promote multiple innate immune antiviral responses. *J Virol*. 89:2575–2589. doi:10.1128/JVI.02791-14.

Rothenburg, S., E.J. Seo, J.S. Gibbs, T.E. Dever, and K. Dittmar. 2009. Rapid evolution of protein kinase PKR alters sensitivity to viral inhibitors. *Nat Struct Mol Biol*. 16:63–70. doi:10.1038/nsmb.1529.

Sadler, A.J., and B.R.G. Williams. 2007. Structure and function of the protein kinase R. *Curr Top Microbiol Immunol*. 316:253–292. doi:10.1007/978-3-540-71329-6_13.

Sheth, U., and R. Parker. 2003. Decapping and Decay of Messenger RNA Occur in Cytoplasmic Processing Bodies. *Science*. 300:805–808. doi:10.1126/science.1082320.

Sheu-Gruttadauria, J., and I.J. MacRae. 2018. Phase Transitions in the Assembly and Function of Human miRISC. *Cell*. 173:946-957.e16. doi:10.1016/j.cell.2018.02.051.

Sidrauski, C., D. Acosta-Alvear, A. Khoutorsky, P. Vedantham, B.R. Hearn, H. Li, K. Gamache, C.M. Gallagher, K.K.-H. Ang, C. Wilson, V. Okreglak, A. Ashkenazi, B. Hann, K. Nader, M.R. Arkin, A.R. Renslo, N. Sonenberg, and P. Walter. 2013. Pharmacological brake-release of mRNA translation enhances cognitive memory. *eLife*. 2:e00498. doi:10.7554/eLife.00498.

Snapp, E.L., N. Altan, and J. Lippincott-Schwartz. 2003. Measuring Protein Mobility by Photobleaching GFP Chimeras in Living Cells. *Current Protocols in Cell Biology*. 19:21.1.1-21.1.24. doi:10.1002/0471143030.cb2101s19.

Stauffer, W., H. Sheng, and H.N. Lim. 2018. EzColocalization: An ImageJ plugin for visualizing and measuring colocalization in cells and organisms. *Sci Rep*. 8:15764. doi:10.1038/s41598-018-33592-8.

Taniuchi, S., M. Miyake, K. Tsugawa, M. Oyadomari, and S. Oyadomari. 2016. Integrated stress response of vertebrates is regulated by four eIF2α kinases. *Sci Rep*. 6:32886. doi:10.1038/srep32886.

Thomis, D.C., and C.E. Samuel. 1993. Mechanism of interferon action: evidence for intermolecular autophosphorylation and autoactivation of the interferon-induced, RNA-dependent protein kinase PKR. *J Virol*. 67:7695–7700. doi:10.1128/JVI.67.12.7695-7700.1993.

Toth, A.M., P. Devaux, R. Cattaneo, and C.E. Samuel. 2009. Protein Kinase PKR Mediates the Apoptosis Induction and Growth Restriction Phenotypes of C Protein-Deficient Measles Virus. *Journal of Virology*. 83:961–968. doi:10.1128/JVI.01669-08.

Yang, W., L.W. Rozamus, S. Narula, C.T. Rollins, R. Yuan, L.J. Andrade, M.K. Ram, T.B. Phillips, M.R. van Schravendijk, D. Dalgarno, T. Clackson, and D.A. Holt. 2000. Investigating Protein−Ligand Interactions with a Mutant FKBP Possessing a Designed Specificity Pocket. *J. Med. Chem.* 43:1135–1142. doi:10.1021/jm9904396.

Yang, Z., A. Jakymiw, M.R. Wood, T. Eystathioy, R.L. Rubin, M.J. Fritzler, and E.K.L. Chan. 2004. GW182 is critical for the stability of GW bodies expressed during the cell cycle and cell proliferation. *J Cell Sci*. 117:5567–5578. doi:10.1242/jcs.01477.

Youssef, O.A., S.A. Safran, T. Nakamura, D.A. Nix, G.S. Hotamisligil, and B.L. Bass. 2015. Potential role for snoRNAs in PKR activation during metabolic stress. *Proc Natl Acad Sci USA*. 112:5023–5028. doi:10.1073/pnas.1424044112.

Zappa, F., C. Wilson, G. Di Tullio, M. Santoro, P. Pucci, M. Monti, D. D'Amico, S. Pisonero-Vaquero, R. De Cegli, A. Romano, M.A. Saleem, E. Polishchuk, M. Failli, L. Giaquinto, and M.A. De Matteis. 2019. The TRAPP complex mediates secretion arrest induced by stress granule assembly. *EMBO J.* 38:e101704. doi:10.15252/embj.2019101704.

Zhou, J., C.Y. Liu, S.H. Back, R.L. Clark, D. Peisach, Z. Xu, and R.J. Kaufman. 2006. The crystal structure of human IRE1 luminal domain reveals a conserved dimerization interface required for activation of the unfolded protein response. *PNAS*. 103:14343–14348. doi:10.1073/pnas.0606480103.

Zhu, P.J., S. Khatiwada, Y. Cui, L.C. Reineke, S.W. Dooling, J.J. Kim, W. Li, P. Walter, and M. Costa-Mattioli. 2019. Activation of the ISR mediates the behavioral and neurophysiological abnormalities in Down syndrome. *Science*. 366:843–849. doi:10.1126/science.aaw5185.

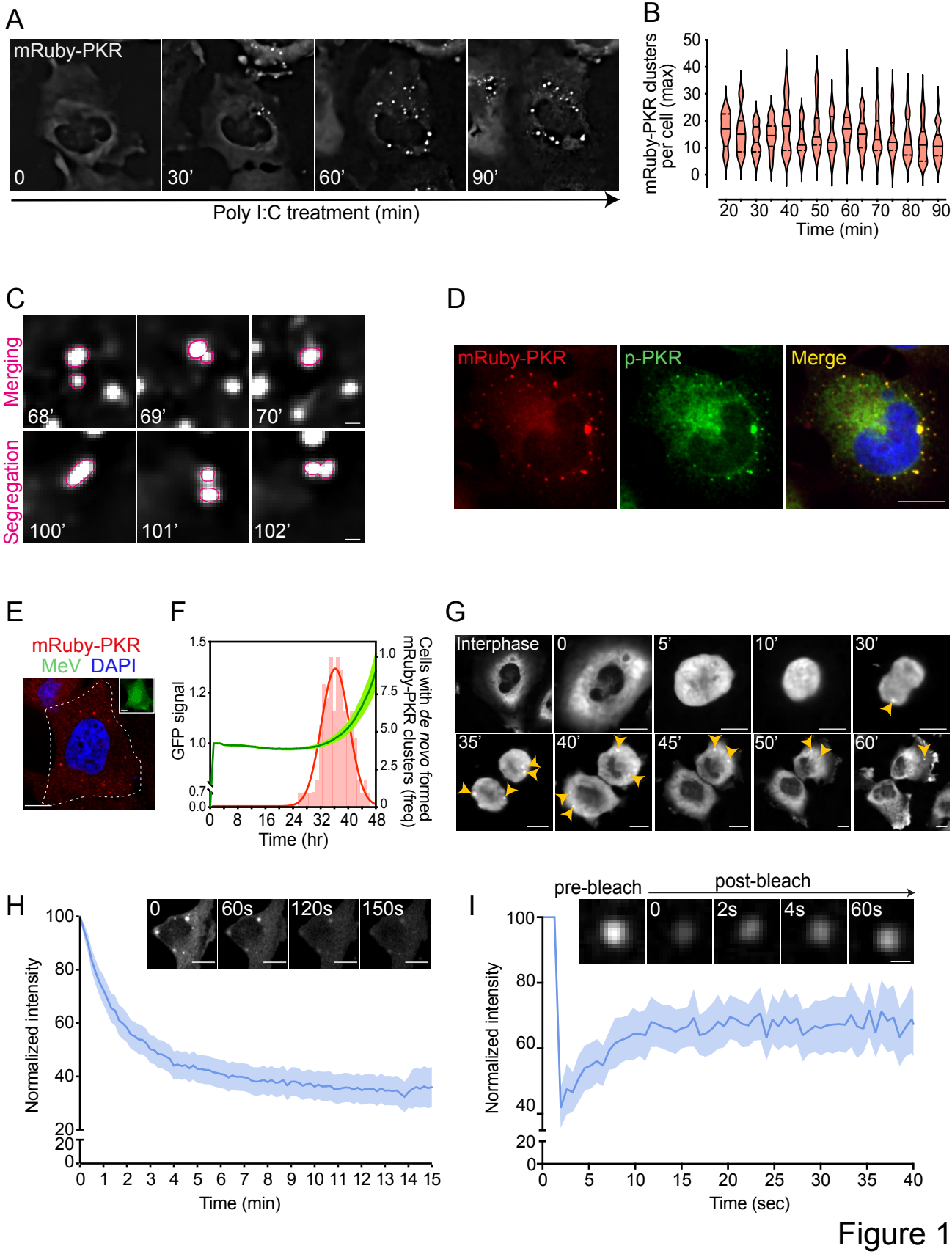
A
mRuby-PKR
0
30'
60'
90'
Poly I:C treatment (min)
B
mRuby-PKR clusters per cell (max)
Time (min)
C
Merging
Segregation
68'
69'
70'
100'
101'
102'
D
mRuby-PKR
p-PKR
Merge
E
mRuby-PKR
MeV DAPI
F
GFP signal
Cells with de novo formed mRuby-PKR clusters (freq)
Time (hr)
G
Interphase
0
5'
10'
30'
35'
40'
45'
50'
60'
H
0
60s
120s
150s
Normalized intensity
Time (min)
I
pre-bleach
post-bleach
0
2s
4s
60s
Normalized intensity
Time (sec)

Figure 1

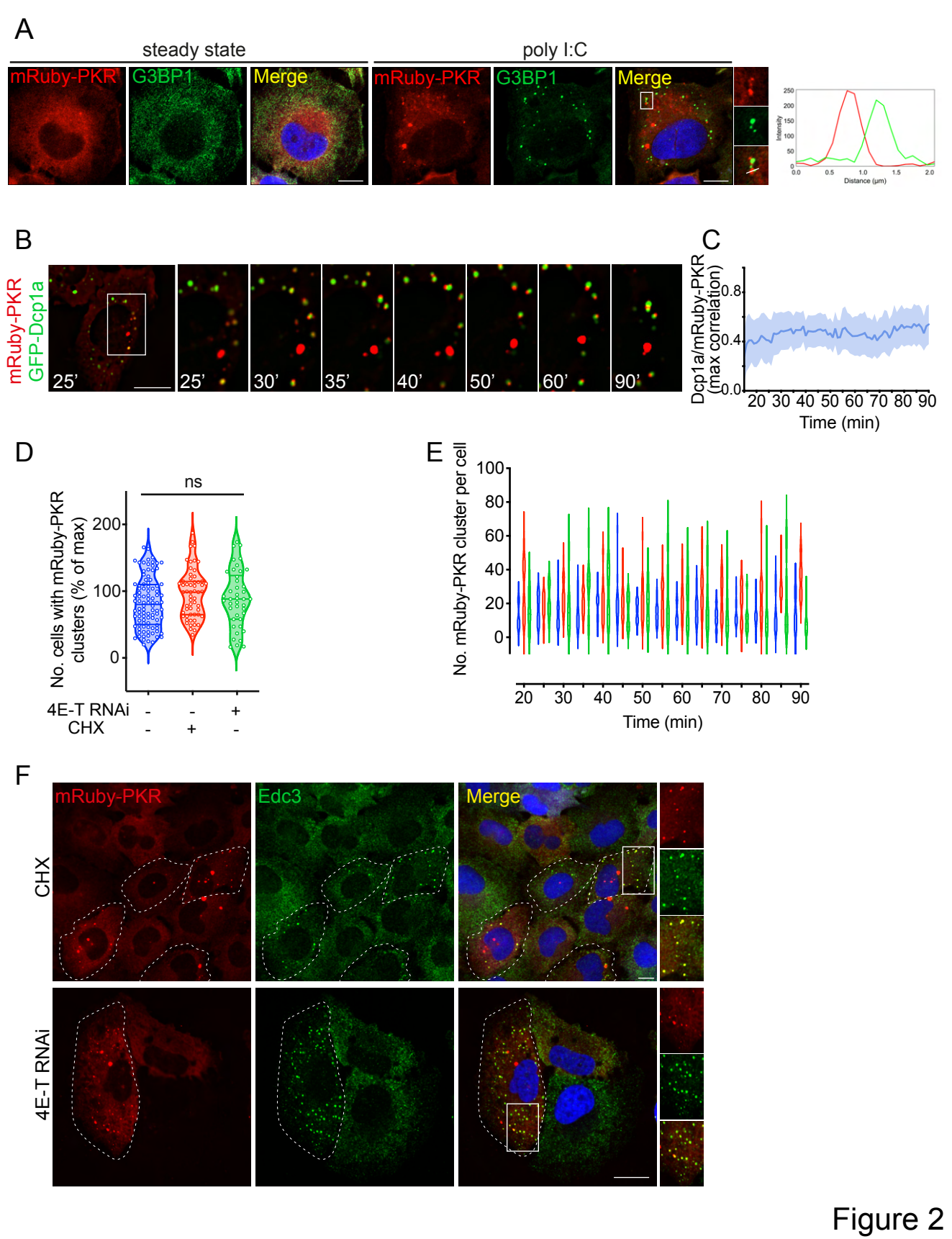
A
steady state
poly I:C
mRuby-PKR
G3BP1
Merge
mRuby-PKR
G3BP1
Merge
Intensity
Distance (μm)
B
mRuby-PKR
GFP-Dcp1a
25'
25'
30'
35'
40'
50'
60'
90'
C
Dcp1a/mRuby-PKR (max correlation)
Time (min)
D
ns
No. cells with mRuby-PKR clusters (% of max)
4E-T RNAi
CHX
E
No. mRuby-PKR cluster per cell
Time (min)
F
CHX
4E-T RNAi
mRuby-PKR
Edc3
Merge

Figure 2

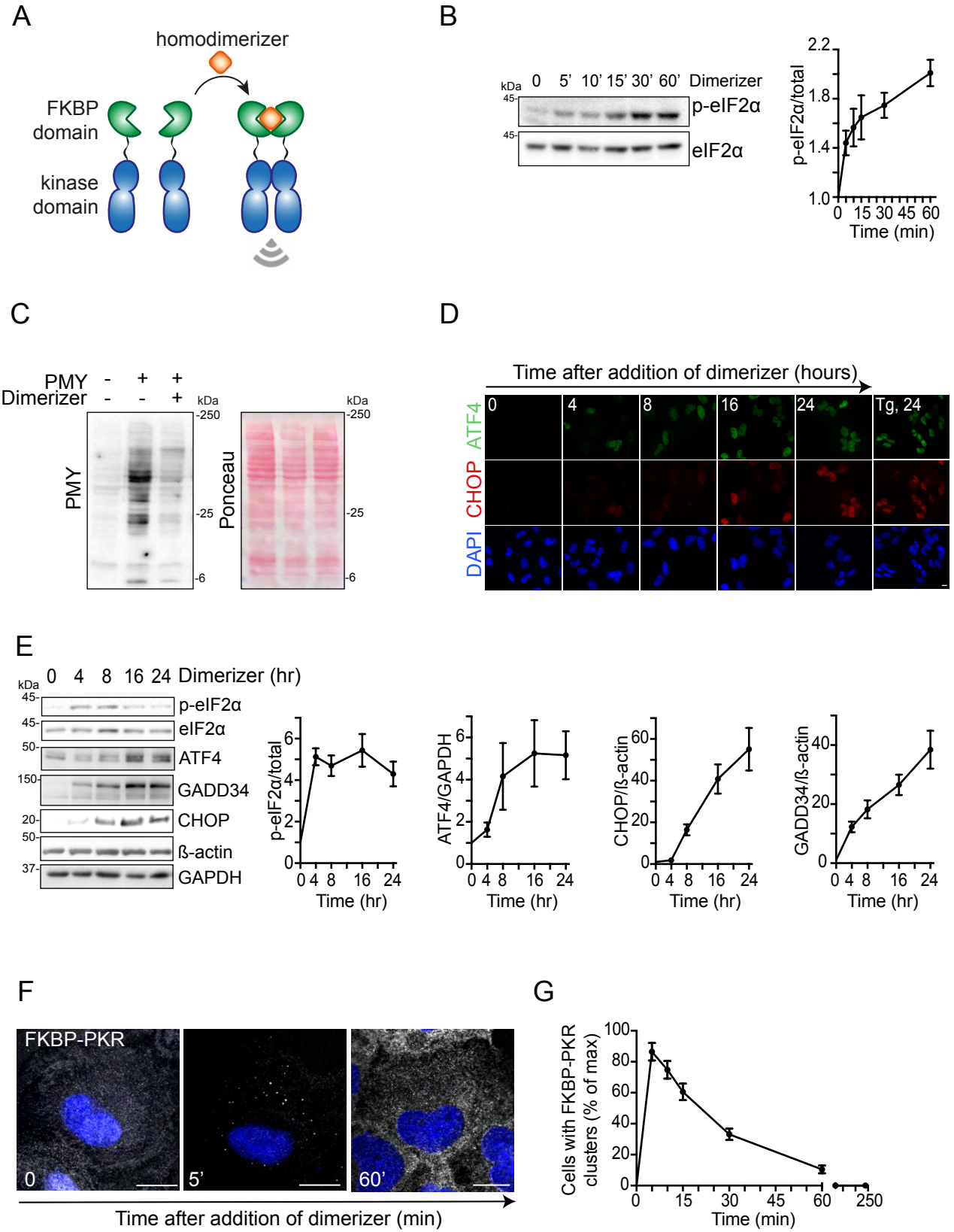
A
homodimerizer
FKBP domain
kinase domain
B
kDa 0 5' 10' 15' 30' 60' Dimerizer
p-eIF2α
eIF2α
p-eIF2α/total
Time (min)
C
PMY - + +
Dimerizer - - +
kDa
PMY
Ponceau
D
Time after addition of dimerizer (hours)
ATF4
CHOP
DAPI
0
4
8
16
24
Tg, 24
E
0 4 8 16 24 Dimerizer (hr)
p-eIF2α
eIF2α
ATF4
GADD34
CHOP
ß-actin
GAPDH
p-eIF2α/total
ATF4/GAPDH
CHOP/ß-actin
GADD34/ß-actin
Time (hr)
F
FKBP-PKR
0
5'
60'
Time after addition of dimerizer (min)
G
Cells with FKBP-PKR clusters (% of max)
Time (min)

Figure 3

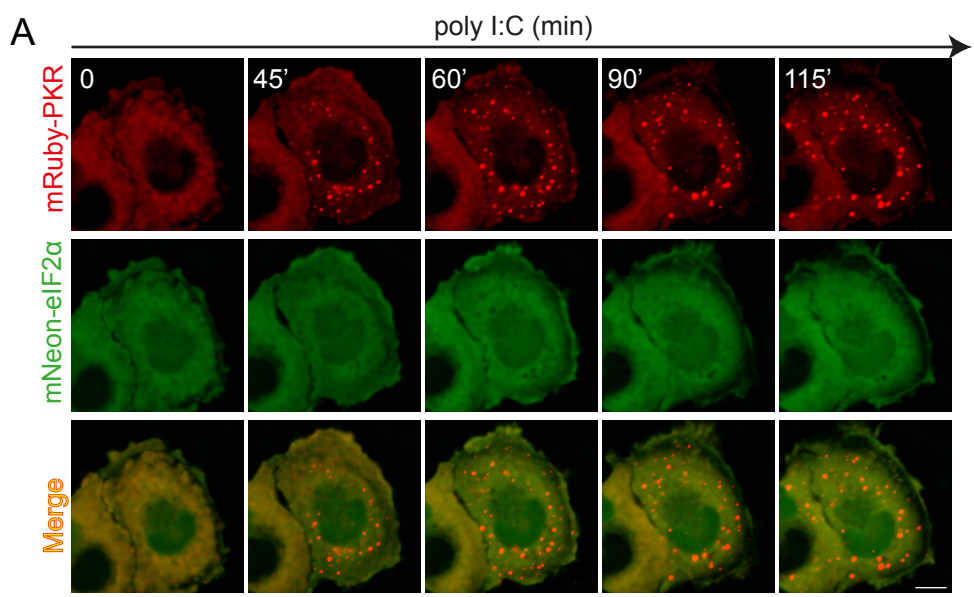
A
poly I:C (min)
0
45'
60'
90'
115'
mRuby-PKR
mNeon-eIF2α
Merge

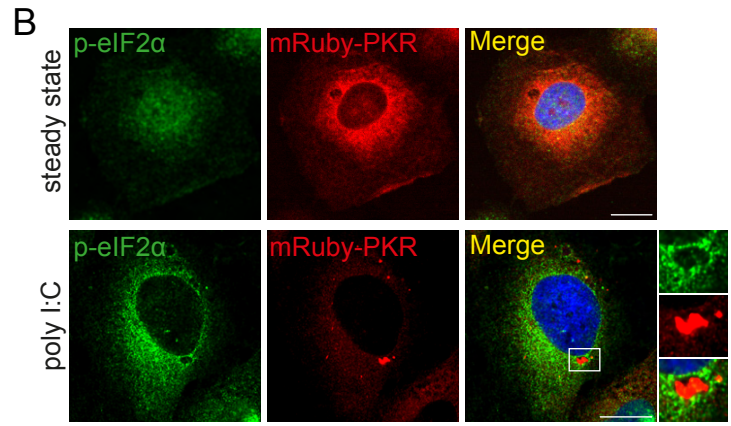
B
p-eIF2α
mRuby-PKR
Merge
steady state
poly I:C

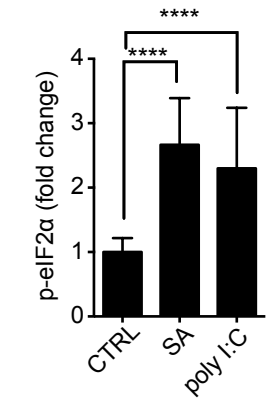
C
****
****
p-eIF2α (fold change)
0
1
2
3
4
CTRL
SA
poly I:C

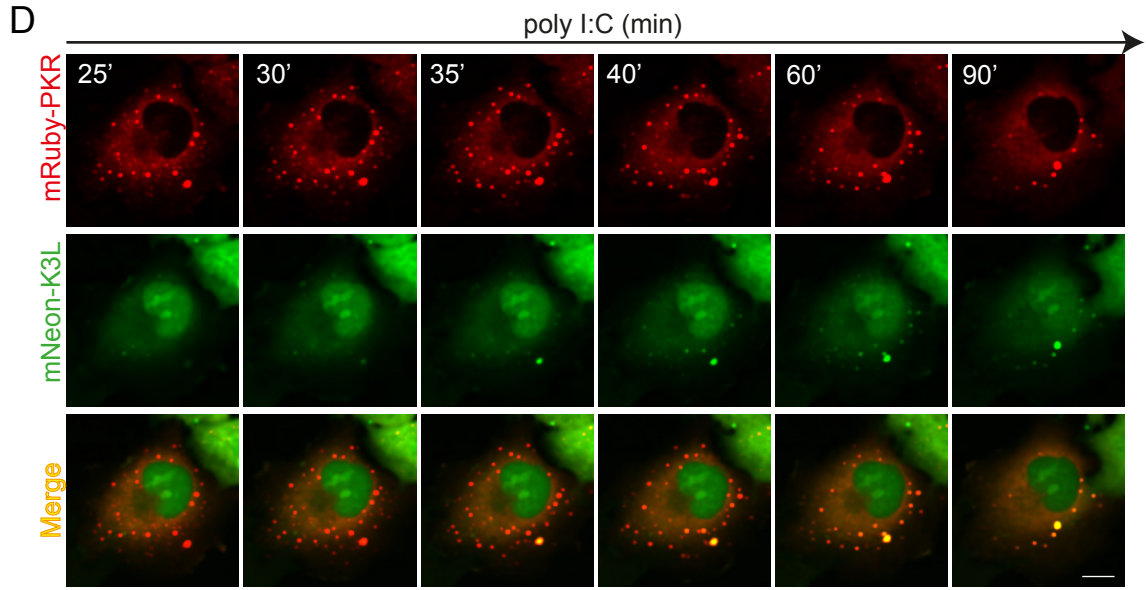
D
poly I:C (min)
25'
30'
35'
40'
60'
90'
mRuby-PKR
mNeon-K3L
Merge

Figure 4

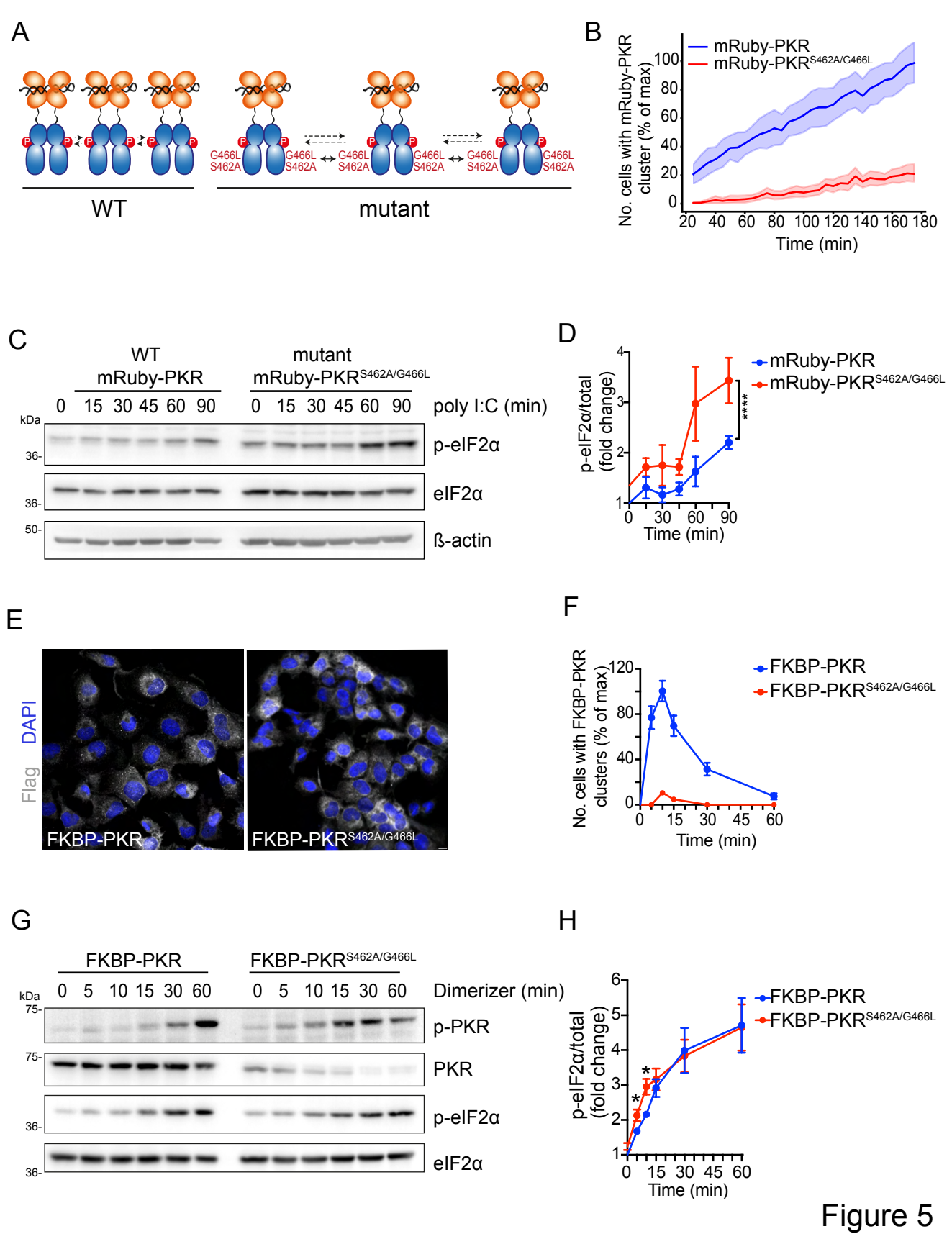
A
WT
mutant
G466L S462A
B
mRuby-PKR
mRuby-PKR S462A/G466L
No. cells with mRuby-PKR cluster (% of max)
Time (min)
C
WT mRuby-PKR
mutant mRuby-PKR S462A/G466L
0 15 30 45 60 90
poly I:C (min)
kDa
p-eIF2α
eIF2α
ß-actin
D
p-eIF2α/total (fold change)
****
Time (min)
E
DAPI
Flag
FKBP-PKR
FKBP-PKR S462A/G466L
F
FKBP-PKR
FKBP-PKR S462A/G466L
No. cells with FKBP-PKR clusters (% of max)
Time (min)
G
FKBP-PKR
FKBP-PKR S462A/G466L
0 5 10 15 30 60
Dimerizer (min)
p-PKR
PKR
p-eIF2α
eIF2α
H
p-eIF2α/total (fold change)
Time (min)

Figure 5

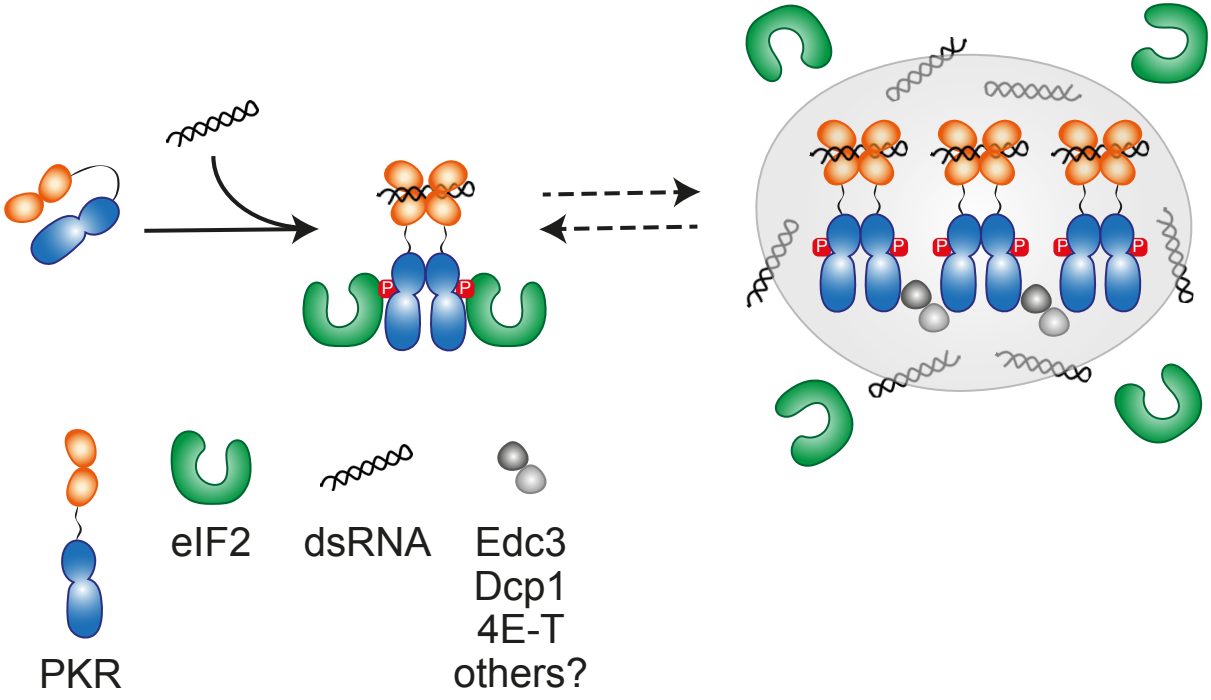

Figure 6